March 18, 1996

FINAL REPORT

Gratings, Inc.
4207 Montgomery Blvd., Suite C
Albuquerque, NM 87109

Contract number : DASG60-95-C-0051

Contract dates : June 1, 1995-Feb. 29, 1996

PI : Saleem H. Zaidi

Title of program : Si wires in SOI configuration

Sponsored By
Ballistic Missile Defense Organization

Managed By
U.S. Army Space and Strategic Defense Command

Disclaimer

The views and conclusions in this document are those of the authors and should not be interpreted as represented the official policies, either expressed or implied , of the government.
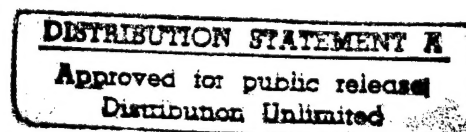
19960408 111

Table of Contents

Si Wires in SOI Configuration

1. Introduction

Si is a poor luminescent material in comparison with direct bandgap semiconductors such as GaAs, or InP. Thus, the room temperature photoluminescence (PL) from porous Si (π-Si) has attracted a great deal of attraction [1]. Although Pickering et al. [2] had previously reported on PL from π-Si attributing it to a complex mixture of phases, i.e., α-Si:O (and / or α-Si:H), the interpretation by Canham and Lehman et al. [3] in terms of quantum-confinement effects has stimulated intense research efforts aimed at a comprehensive understanding of the underlying physical mechanisms. To date, however, a clear picture has yet to emerge.

Research efforts have focused on quantum-confinement [4-6], alternate chemical mechanisms, i.e., Si-H$_x$ complexes [7-8], and surface-states mechanism [9]. Precise interpretation is further complicated by the fact that π-Si PL exhibits two bands with widely different response times : orange-red (850-650 nm) PL decaying at time scales $\sim$ 10 μsec, and blue-green (420-540 nm) PL with a much faster (ns) decay rate [10]. This blue emission has also been attributed to SiO$_x$ (x~1.4-1.6) complexes [11]. In an extensive review of π-Si optical properties by D. J. Lockwood [12], several different sources of PL in anodized Si were analyzed with a tentative conclusion that the red emission originated from quantum-size related effects. Lockwood, however, pointed out that a definitive explanation of the various light-emitting sources in π-Si will only follow from a careful investigation of the surface chemistry of pores, defects in Si crystallites, and uniform Si wires, or dots so as to minimize the inhomogeneous broadening effects.

Porous Si formed by anodization [2] has a complex 3-D structure that makes it difficult to isolate chemical effects from crystal-size effects. Lithographic techniques offer an attractive alternative for fabrication of uniform, nanocrystalline structures. Liu et al. [13] and Fischer et al. [14] have applied electron and ion-beam lithographic techniques to form 2-D columnar structures. These techniques, however, are slow, expensive, and difficult to extend to large areas. We have developed fabrication techniques to form crystalline structures $\sim$ 5-10-nm dimensions by combining interferometric lithography with the etching of Si and its thermal oxidation. This SBIR phase I project report presents a detailed investigation of fabrication of free-standing Si Wires and their characterization (optical and electrical) as wire diameters are reduced to $\sim$ 10 nm. The project report is divided into the following sections ; section 2 describes the nanofabrication techniques in Si, section 3 describes the Raman response as a function of the crystal size, section 4 presents the PL measurements from nanoscale Si wires embedded in thermally grown oxide films, section 5 presents detailed electrical characterization of Si, the results are summarized and discussed in section 6, and the finally the references in section 7.

2

2. Nanostructure Fabrication

Interferometric lithography provides an inexpensive method of fabrication of nanoscale periodic structures over large areas. Interference effects between two coherent laser beams produce a simple periodic pattern with period d = $\lambda/2\sin\theta$, where λ is the wavelength of the exposing beam, and 2θ is the angle between the two intersecting beams [15-16]. Grating patterns are first formed in positive photoresist (1350B-SF). Following photoresist exposure and development, the grating pattern is transferred to either an oxide, nitride, or a metal film using etching or lift-off processes to act as a mask during Si etching. Room temperature wet-chemical etching in Si is carried out in 40 % wt KOH solution. KOH etching is anisotropic and the etched profiles are crystal-orientation dependent, an extensive review of wet-etching in (100) and (110) Si is provided by Bassous [17] and Bean [18].

Figure 1 shows an experimental configuration used for fabricating grating structures. An expanded laser beam from a single-mode Ar-ion laser (λ=488, 365, or 257 nm) is incident on a Fresnel mirror (FM) arrangement [19] mounted on a rotation stage to vary grating period. Figure 2 shows a scanning electron microscope (SEM) picture of
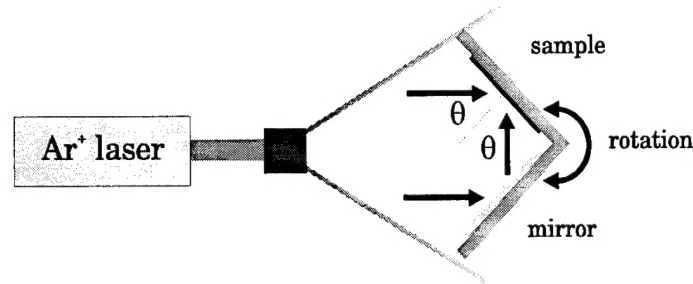

Fig. 1 Experimental configuration for interferometric grating fabrication.

a 0.47-μm grating period etched in (100) Si. The depth of the grating structure is limited by the intersection of the two <111> planes which stops any further vertical etching [17-18]. Figure 3 shows another SEM picture of a 0.36-μm period grating etched in (110) Si. These type of very high aspect ratio gratings can only be fabricated in (110) Si because of the extreme etch rate anisotropy (1:400) between the perpendicular <111> and <110> planes [20-21]. Cross-sectional TEM images of these structure show that the sidewalls are nearly perfect; the lines visible in the SEMs correspond to nearly atomic steps. The transverse dimensions of these atomic steps are expected to be of significance in reduced (~ 10 nm) crystalline sizes.

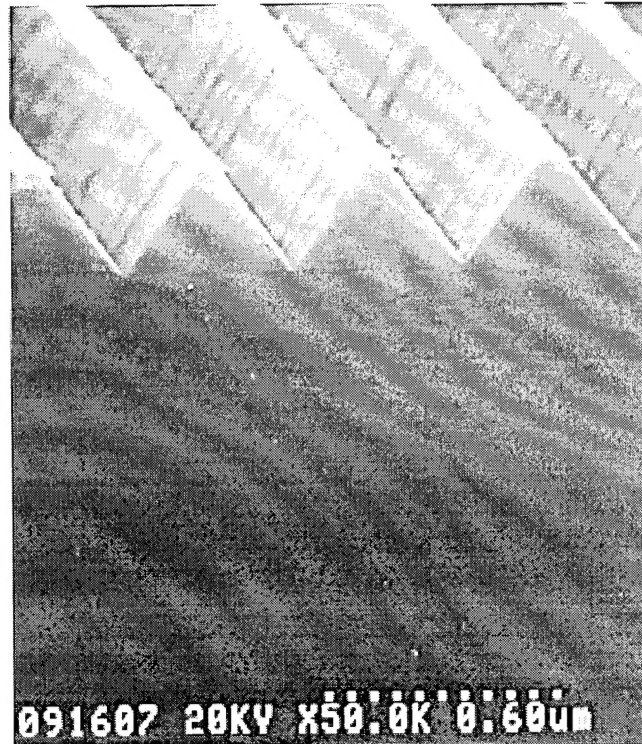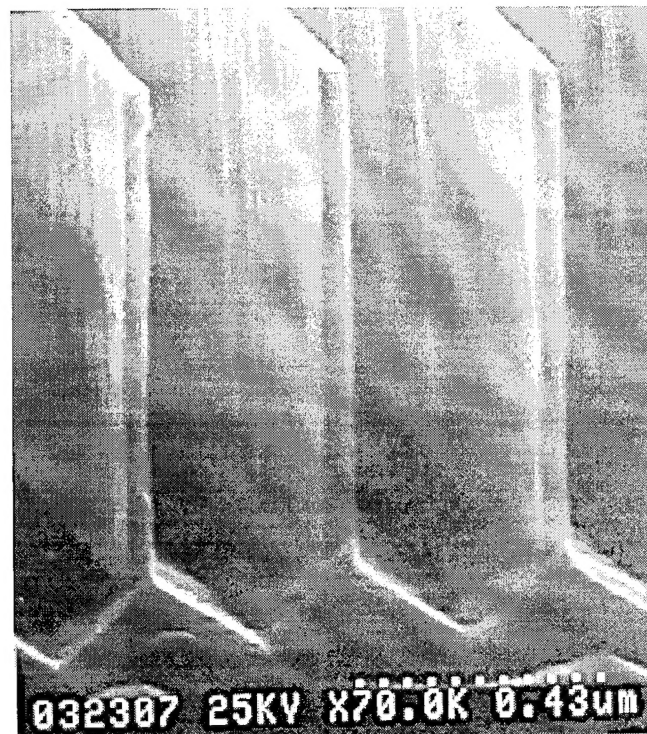Fig. 2 SEM picture of a 0.47-μm period grating etched in (100) Si.

Fig. 3 SEM picture of a 0.36-μm period, 50-nm linewidth (110) Si structures fabricated by KOH etching.

For investigations of Si quantum-size effects, crystal dimensions have to be reduced to ~ 5-10 nm. A convenient way to do so is by conventional furnace oxidation of Si [22]. Such an oxidation treatment will produce quantum-sizes in (110) grating structures as shown in Fig. 4, where a controlled oxidation process has been carried out to form ~ 10-nm linewidth grating structures. A more detailed discussion of these structures to form free-standing wires will be a part of phase II proposal. This oxidation treatment will not produce quantum-sized structures in (100) Si that are isolated from the rest of the substrate. One alternative, which formed the basis of our phase I SBIR proposal, and is also the subject of detailed measurements reported here, is to use commercially available SOI (Si on insulator) wafers as the starting material. A typical SOI structure consists of a top crystalline Si film of a specified thickness separated from the Si substrate underneath by a thick thermally grown oxide film. This has the advantage that if the top Si film thickness is less than the total etched depth of a grating, i.e., less than 0.3 μm in Fig. 2, the grating lines become isolated from each other, and further oxidation to reduce linewidths will result in formation of isolated Si wires embedded in the oxide film. Fig. 5 shows a cross-sectional view of a typical SOI structure. The Si film of ~ 0.18-μm thickness is sandwiched between two thermally grown oxide films. The thick oxidation process had been used to reduce top Si thickness from ~ 0.5-μm to 0.18 μm. Fig. 6 shows another example of such a process to reduce Si thickness to ~ 0.08 μm. Application of SOI material to form Si wires had been previously reported by Potts et al. [23-24]. Using electron-beam lithography techniques and dry etching of (100) Si, they fabricated wires varying in diameter from 1.0 μm to 70 nm, and lengths ~ 40 μm. Using e-beam lithography and wet-chemical etching of (100) and (110) Si, Itoh et al. [25] also reported on fabrication of wires in SOI structures. Their wire dimensions were ~ 0.2 X 0.2 μm^2.

We have applied much simpler and economical interferometric lithography techniques to form wires in (100) Si with diameters varying from ~ 0.6 μm to ~ 10 nm. By appropriate combinations of top Si thickness and its wet, or dry etching, a variety of wire profiles can be fabricated. Figs. 7 a-c shows a sequence of 0.75-μm period structures formed by KOH-etching and subsequent oxidation processes. Fig. 7a shows the as fabricated structure in which the KOH etching was carried out with a ~ 40-nm Cr film mask. The top Si film thickness was ~ 0.3 μm, and KOH etching results in a triangular structure with <111> sidewalls as would be expected for Cr-film mask aligned along the [110] direction. Fig. 7b shows the same structure following a thin (~ 0.13 μm) oxidation to reduce Si linewidths. The oxidation was carried out in a furnace at ~ 1000° C using O$_2$ at ~ 3 sccm. Notice that the oxidation process tends to smooth out the sidewalls. For the quantum sizes being investigated here, the wire diameters have to be reduced by at least two orders of magnitude by oxidation treatments. Fig. 7c shows an example of the same structure following oxidation to form ~ 10-nm diameter wires. For Si sizes in this range, SEM measurements are not very accurate because the focused e-beam spot tends to oxidize the remaining Si (which is not very much to start with). However, in Fig. 7c, it is still possible to see very fine triangular structure at the center of the thick (~ 0.2 μm) thermally grown oxide film. Using a CCl$_2$F$_2$-based reactive ion etching (RIE) process, we have formed rectangular-to-square wire profiles. Figs. 8 a-c show a sequence of 0.75-μm period structures subjected to same oxidation process as in Figs. 7 b-c. Fig. 8a shows the as fabricated structure after RIE process using ~ 40-nm Cr film. The grating linewidth was ~ 0.44 μm, and Si thickness ~ 0.3 μm. Fig. 8b shows the results of a thin oxidation, and Fig. 8c shows results of oxidation to form ~ 10 nm rectangular-cross-section wires. In this case, the Si wires are not possible to distinguish because of SEM-induced oxidation. Finally, Figs. 9 a-c shows the sequence of wire fabrication in thicker ~ 0.43 μm Si films. The as-fabricated RIE-etched structure in Fig. 9a shows significant deviation from a vertical profile, but still it is seen that all grating lines are separated. Figs. 9 b-c show the results of oxidation, notice that the cross-sectional profile in Fig. 9b maintains the profile of Fig. 9a and also has smoother sidewalls. The same profile is maintained in

5

Fig. 4 SEM picture of an oxidized Si (110) grating to form ~ 10-nm linewidth crystalline Si structures shown as dark lines embedded in thermally grown oxide film.
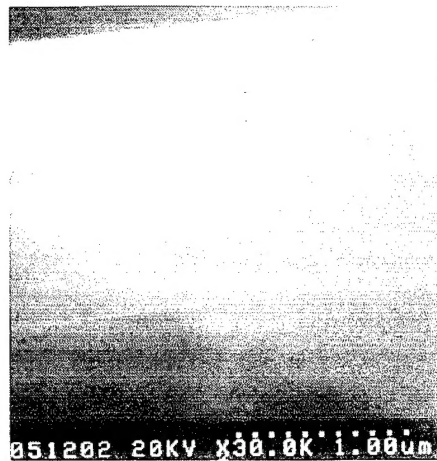

Fig. 5 SEM picture of a conventional SOI structure, Si film of ~ 0.18-μm thickness is sandwiched between two thick oxide films.
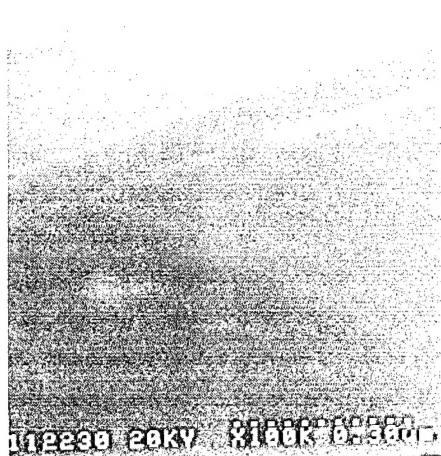

Fig. 6 SEM picture of another SOI structure showing ~ 0.08-μm thick Si film.

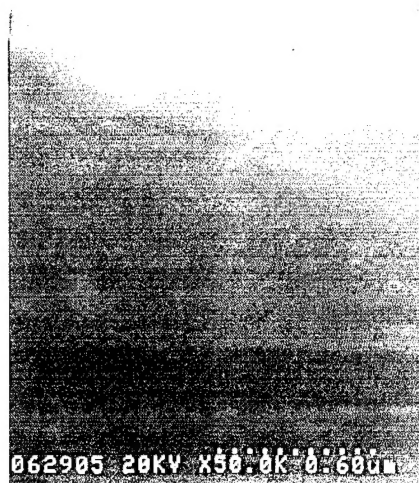Fig. 7a SEM picture of a 0.75-μm period Si (100) grating formed by KOH etching in SOI configuration.

Fig. 7b SEM picture of the grating shown in Fig. 7a following ~ 0.18-μm thick oxidation.

Fig. 7c SEM picture of grating structure shown in Fig. 7a following oxidation processes to form ~ 10-nm wire diameters.

Fig. 8a SEM picture of a 0.75-μm period Si (100) grating formed by RIE in SOI configuration.

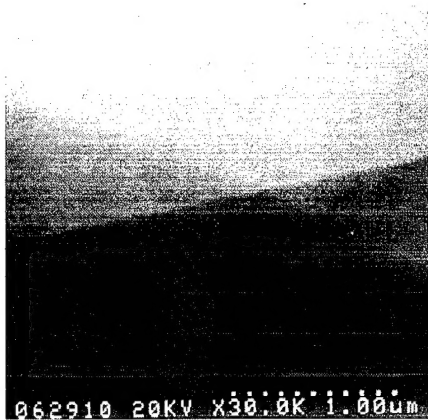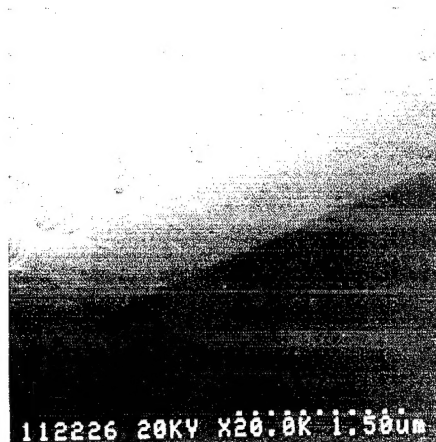Fig. 8b SEM picture of the grating shown in Fig. 8a following ~ 0.18-μm thick oxidation.

Fig. 8c SEM picture of grating structure shown in Fig. 8a following oxidation processes to form ~ 10-nm wire diameters.

Fig. 9a SEM picture of a 0.75-μm period Si (100) grating formed by RIE in ~ 0.43-μm thick Si film in SOI configuration.

Fig. 9b SEM picture of the grating shown in Fig. 9a following ~ 0.18-μm thick oxidation.

Fig. 9c SEM picture of grating structure shown in Fig. 9a following oxidation processes to form ~ 20-30-nm wire diameters.
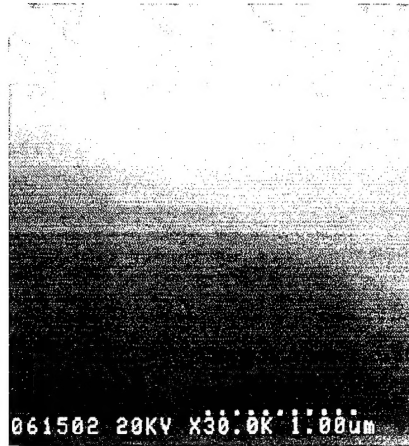
wire diameters varying from ~ 0.02-0.03 µm as shown in Fig. 9c.

In summary, these results demonstrate that using inexpensive processing steps that are compatible with Si microelectronics, large area crystalline Si wires with diameters ~ 10 nm can be routinely fabricated. In addition, by a suitable combination of Si film thickness and the etching process, cross-sectional profiles of the wires can be easily varied from triangular to square.

3. Raman Scattering Measurements

The optical response of these nanoscale linewidth Si wire structures has been investigated by Raman scattering (RS) measurements. RS has been previously used to characterize Si crystal size variations in π-Si [26-27], spherical particles embedded in oxide matrix [28-29], and laser-annealed amorphous films [30]. Goodes et al. [27] showed that for π-Si, Raman mode consisted of a single peak at ~ 520 cm^{-1} (corresponding to bulk Si) plus a broad tail extending to low frequencies that was attributed to crystal sizes < 10 nm. Splitting of the Raman mode has also been observed [26]. Similar features have been reported from Si spherical particles and laser-annealed amorphous films [28-30].

Room temperature Raman scattering measurements reported here were recorded in back-scattering geometry using a 40 x objective to focus 488-nm beam onto the sample (~ 10-µm spot size). Spectra were analyzed with a 3/4-m spectrometer and a cooled GaAs photomultiplier with photon-counting electronics. Fig. 10 shows a series of RS measurements from grating structures shown in Figs. 7a, 8a, & 9a. The sharp line feature at ~ 530 cm^{-1} represents a laser plasma line that serves as an absolute alignment marker in determining the small shifts of the Raman mode. Fig. 10a shows RS measurements from ~ 0.3-µm thick film in SOI configuration, for comparison RS measurement from the bulk Si under identical conditions is also plotted. It is seen that the RS signal intensity from the thin film is about 2-1/2 times smaller than the bulk Si, in addition, its FWHM is increased to ~ 4.4 cm^{-1} in comparison with ~ 3.3 cm^{-1} for bulk Si. This reduction in signal intensity and broadening is attributed to Boron doping of the SOI samples and is consistent with similar results reported in literature [31-32]. Also the undoped SOI samples showed linewidths similar to bulk Si. Fig. 10b shows the RS signal from as-fabricated KOH-etched gratings from which the Cr etch mask has been removed (see Fig. 7a). The FWHM of this structure is similar to the 0.3-µm film, however, the signal intensity has been enhanced by a factor of 4. This enhancement can be attributed to a combination of the increased surface area and roll-off in Boron concentration from top surface to the Si/SiO$_2$ interface. Fig. 10c shows that the RS measurements for the 70-min. RIE sample (Fig. 9a). Again, the FWHM is similar to the 0.3-µm film, the signal intensity, however, is enhanced by a factor of 8. The increased enhancement in comparison with Fig. 10b here is attributed to the increased Si film thickness (from 0.3 to 0.43 µm), surface area, and the reduction of Boron-concentration from the top surface to the Si/SiO$_2$ interface.
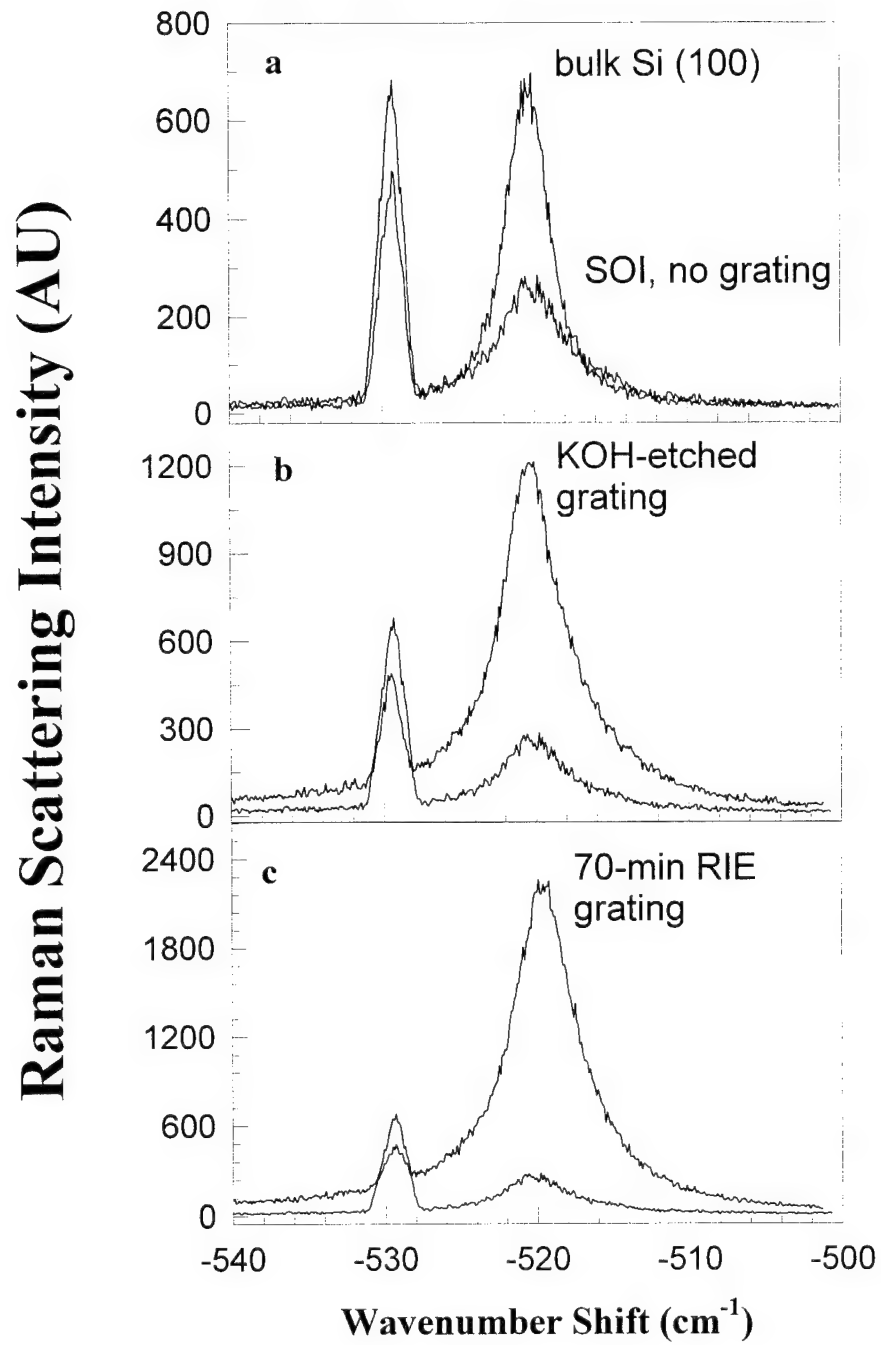
Fig. 10 Raman scattering measurements from KOH and dry etched gratings in SOI configuration.

Fig. 11 shows RS measurements following ~ 0.13-μm thick oxidation, for comparison the RS measurement from the thin 0.3-μm film without wires is also plotted on the same scale. The profiles of the wire structures following this oxidation step are shown in Figs. 7b, 8b, & 9b. Signal intensity enhancement varies from ~ 2.8, 4.7, and 2.4 for KOH-etched (Fig. 11a), 0.3-μm thick RIE (Fig. 11b), and 0.43-μm thick RIE samples respectively. Another very distinctive feature of these measurements is the high-frequency shifts of the Raman mode ~ 1.4 cm^{-1} in Fig. 11c. High frequency shifts of the bulk Raman mode have been reported for Si films grown on Sapphire (SOS) [33-34]. For these SOS films grown at ~ 1000° C, the thermal expansion coefficient of Sapphire is ~ 2.5 times larger than the Si film, which results in a compressive strain at the Si/Sapphire interface. This compressive strain is reflected in high-frequency shifts of the Raman mode by ~ 3 cm^{-1}, and broadening by ~1.5 cm^{-1}. For Si films grown on vitreous quartz, the expansion coefficient of Si is ~ 6 times larger than quartz resulting in tensile strain at the Si/quartz interface. This tensile strain is reflected in low-frequency shift of ~ 6 cm^{-1}, and broadening by ~ 3 cm^{-1} [33]. The broadening in both cases has been attributed to finite crystal sizes in the as-grown films [35]. For the oxidized Si wires shown in Figs. 7b, 8b, & 9b, a low-frequency shift of the Raman mode is expected, therefore, the high-frequency shift actually observed presents an anomaly that needs to be investigated in more detail.

For Si wire dimensions reduced to ~10-20 nm diameters by oxidation shown in Figs. 7-9c, a number of interesting features are observed. Fig. 12 shows RS measurements from the RIE samples shown in Figs. 8c & 9c. Fig. 12a shows that the Raman lineshape is symmetrically broadened to ~ 6.3 cm^{-1}, the peak frequency is up-shifted by ~ 2 cm^{-1}, and signal enhancement is reduced from 4.7 to 2.7 times the intensity of the bulk SOI sample. Figs. 12b & c show the RS measurement from wire diameters estimated to ~ 10 nm. For such fine structures, a splitting of the Raman mode is observed. This slitting is better seen in Fig. 12c, where the high-frequency shift is ~ 3.4 cm^{-1}. By subtracting the background bulk SOI signal from the wires, Raman response of the wires alone can be evaluated. Fig. 13 shows the RS measurements of Fig. 12 following this subtraction process. Fig. 13a shows both the low- and high-frequency peaks, Figs. 13b-c show single broad peak up-shifted by ~ 3.4 cm^{-1} and broadened to ~ 4.4 cm^{-1}. Fig. 14 shows RS measurements from KOH-etched wires thinned to ~ 10-20 nm by conventional oxidation. Fig. 14a shows asymmetric lineshape, Figs. 14b-d show increasing asymmetry, high-frequency shifts, and a splitting of the bulk mode. Fig. 15 shows the same results following background subtraction of the bulk SOI signal. Again, we observe an evolution of the Raman mode from asymmetry to splitting of the bulk mode. The broad low-frequency peak in Fig. 15d is down-shifted by ~ 5 cm^{-1}, while the stronger and narrower frequency peak is up-shifted by 2.5 cm^{-1}.

The Raman scattering measurements shown in Figs. 12-15 are consistent with the first-principles calculations reported by Kanellis et al. [36]. They calculated the frequencies of the long wavelength optical modes of thin slabs of Si, and predicted a splitting of the 3-fold generate bulk Raman mode for thickness below 10 nm. The
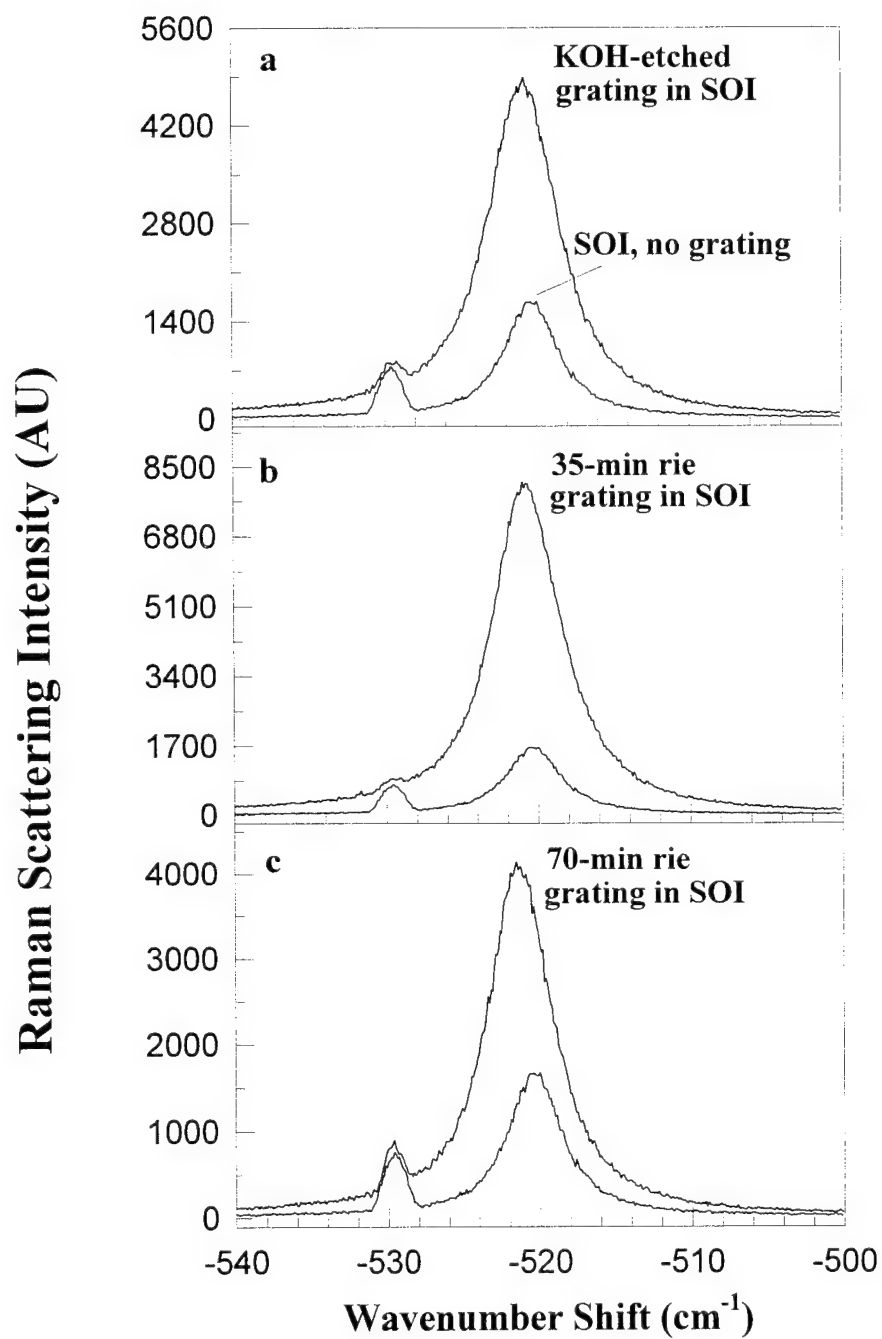
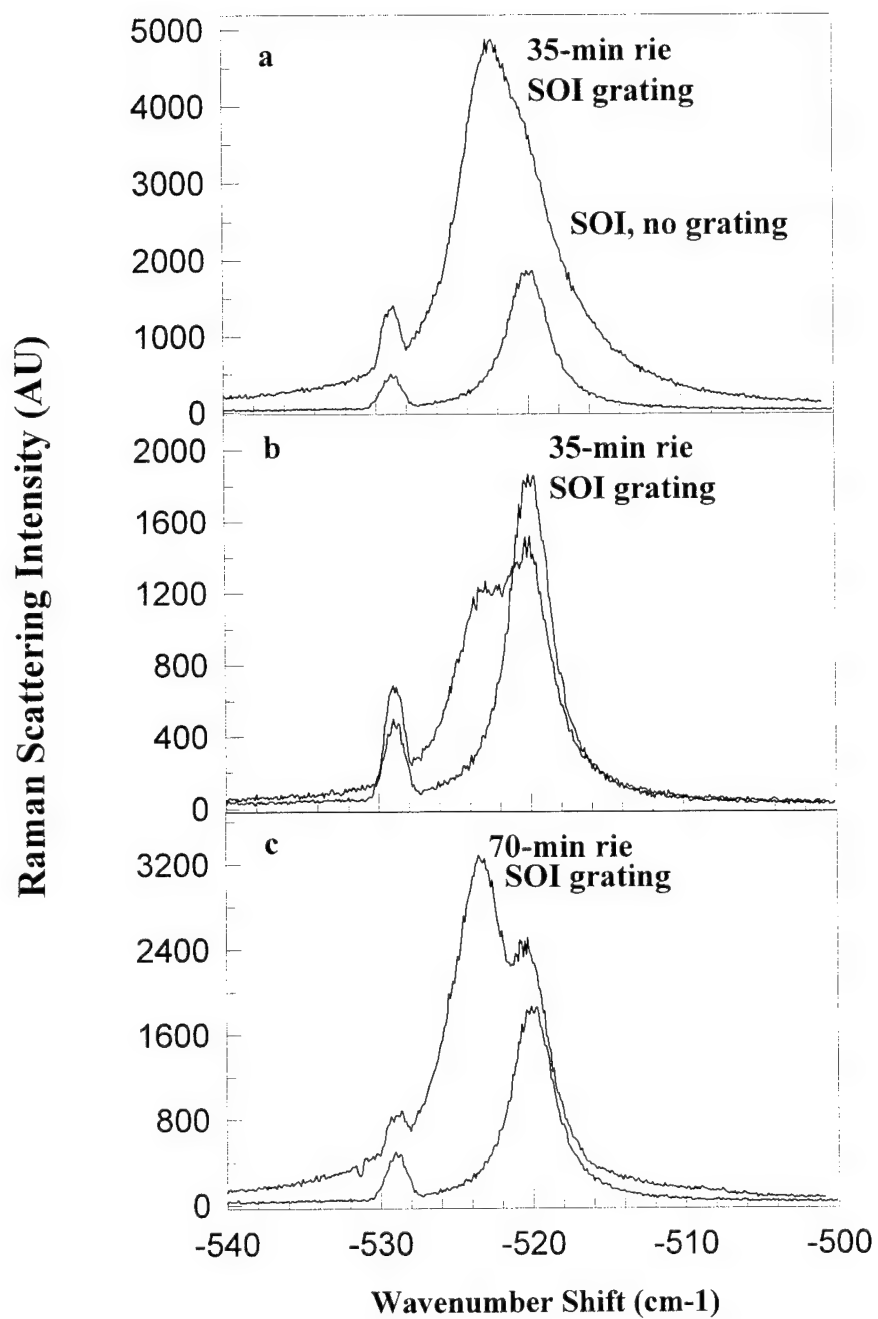Fig. 11 Raman scattering measurements from oxidized KOH and dry etched wire structures.

Fig. 12 Raman scattering measurements showing a high-frequency shift.
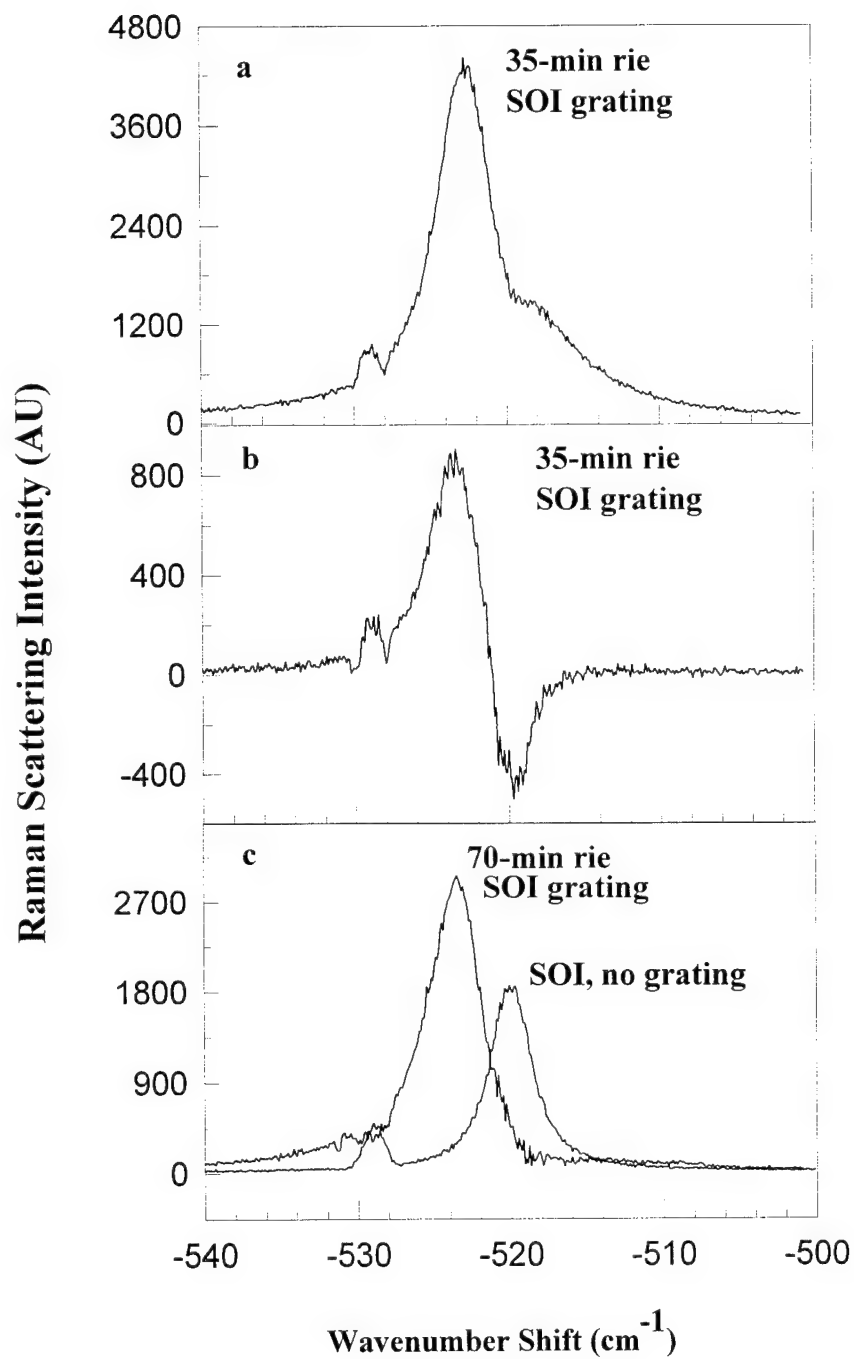
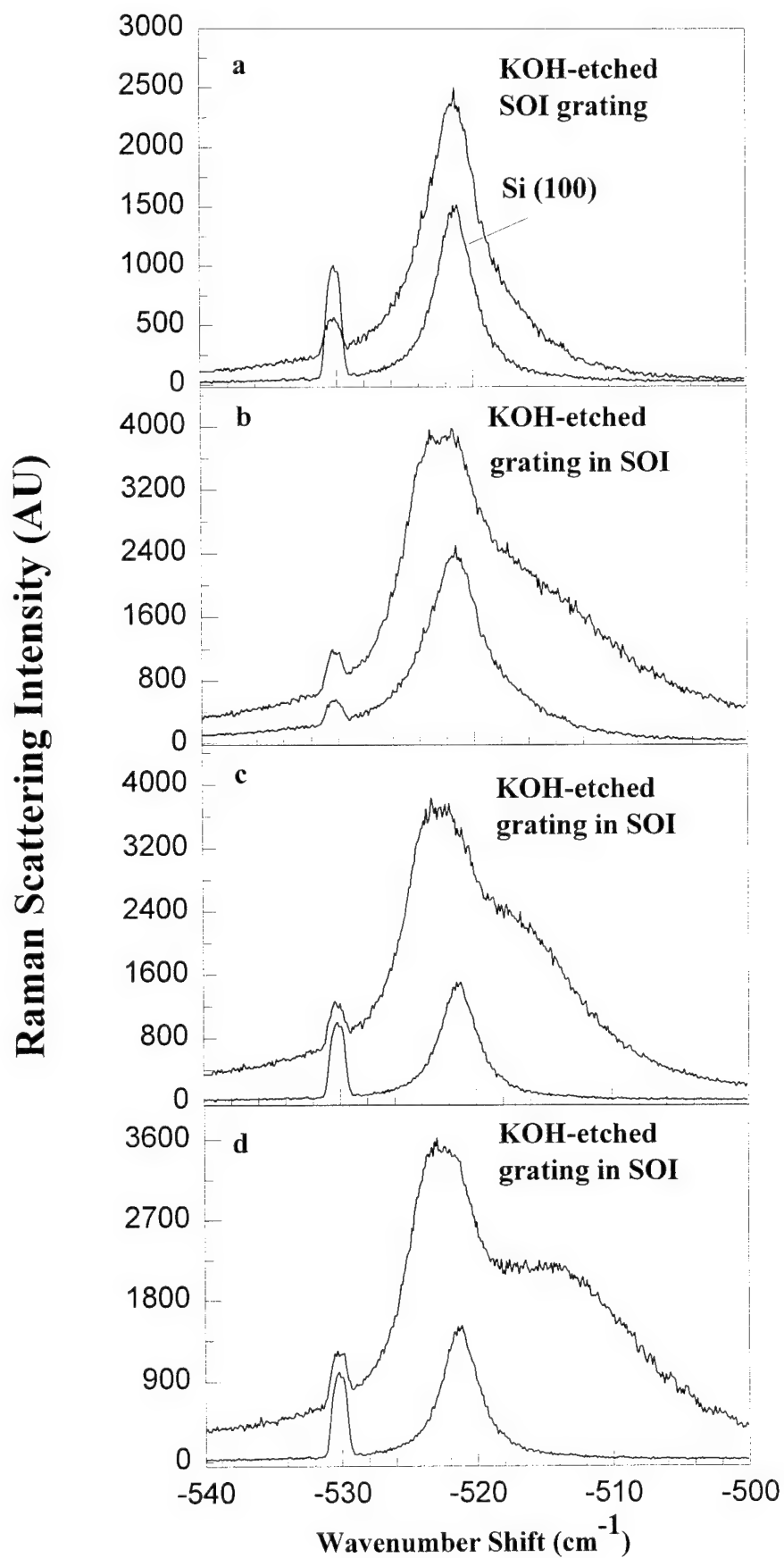Fig. 13 Raman scattering measurements showing the difference signal.

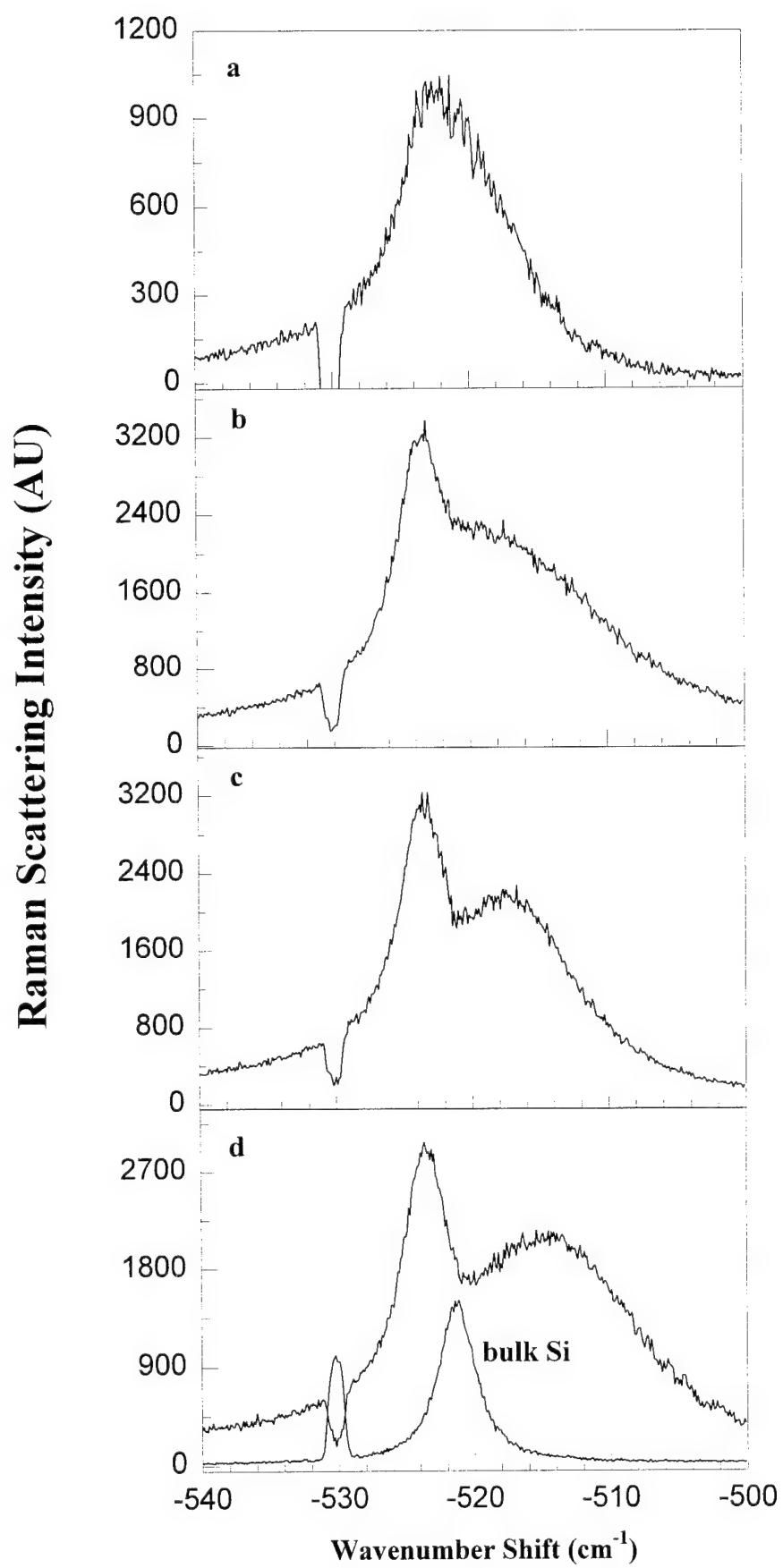Fig. 14 Raman scattering measurements showing splitting of the Raman mode.

Fig. 15 Raman scattering measurements showing the difference signal.

17

low-frequency shifts of the Raman mode seen in Figs. 13a & 15d agree well with these calculations, however, the narrow up-shifted peaks are not explained by their model. This may have been due to the fact that the model calculations were done for free Si surface, while for the wires investigated here, the Si surfaces are covered in thermally grown oxide and have steps on sidewalls. More detailed investigations are required for a complete understanding of the evolution of Raman mode for these quantum-sized wire structures.

In summary, Raman scattering measurements have been shown to be a sensitive function of the wire diameters down to ~ 10 nm. There are still unexplained features such as the Raman splitting between low and high frequency peaks, and will be investigated in more detail in phase II.

4. Photoluminescence Measurements

Room temperature PL measurements were carried out for CW 257-nm excitation (intracavity doubled Ar-ion laser) in a back-scattering geometry using a real-time OMA (optical multi-channel analyzer) system equipped with a 1/4-m spectrometer and an IR enhanced thermoelectrically cooled CCD camera. For system calibration, we evaluated the PL from the quartz beam splitter used in our optical collection setup. The PL from the beam splitter was very weak and broad band in comparison with the PL from wires. In all measurements, this background signal was recorded under identical conditions and subtracted from the actual signal from wires to eliminate background effects.

Measurements were carried out over a wide range of Si wire diameters, profiles, and heights. Significant PL was measured only from samples with ~ 10-nm wire cross-sections irrespective of their periods, or profiles. All measurements reported here were carried out for Si wires embedded in thermally grown oxide films. Figs. 16 & 17 show characteristic photoluminescence from KOH-etched wires. Fig. 16a shows that the luminescence is broad with a peak ~ 570 nm, and FWHM ~ 110 nm, the cut-offs at 360 and 760 nm are instrumental. Figs. 16 b&c show the spectra from the same sample following prolonged air exposure (~ 1-2 weeks). Interesting feature of these measurements is the evolution of the narrow line at ~ 380 nm, the other sharp line at ~ 760 nm represents the second order of this 380 nm line. Also notice that the PL peak in Fig. 16c is also shifted to ~ 490 nm. Figs. 17 a-c show a series of PL measurements from the another KOH-etched wires sample demonstrating that the broad asymmetric PL in Fig. 17a is actually composed of several narrow line centered at ~ 400, 460, 540, and 650 nm respectively. Figs. 18 & 19 show PL measurements from reactively ion-etched wires. Fig. 18a shows PL lineshape (similar to KOH-etched wires shown in Fig. 17a) from 70-min. RIE wires with a peak at ~ 480 nm, and shoulders at ~ 460 and 540 nm, and the narrow line at ~ 380 nm (Fig. 17b). Fig. 19 shows a series of PL measurements from the 35-min. RIE wires. The PL lineshape is similar to Fig. 16a for KOH wires, the narrow line at 380 nm and its second order at 760 nm are also the same.
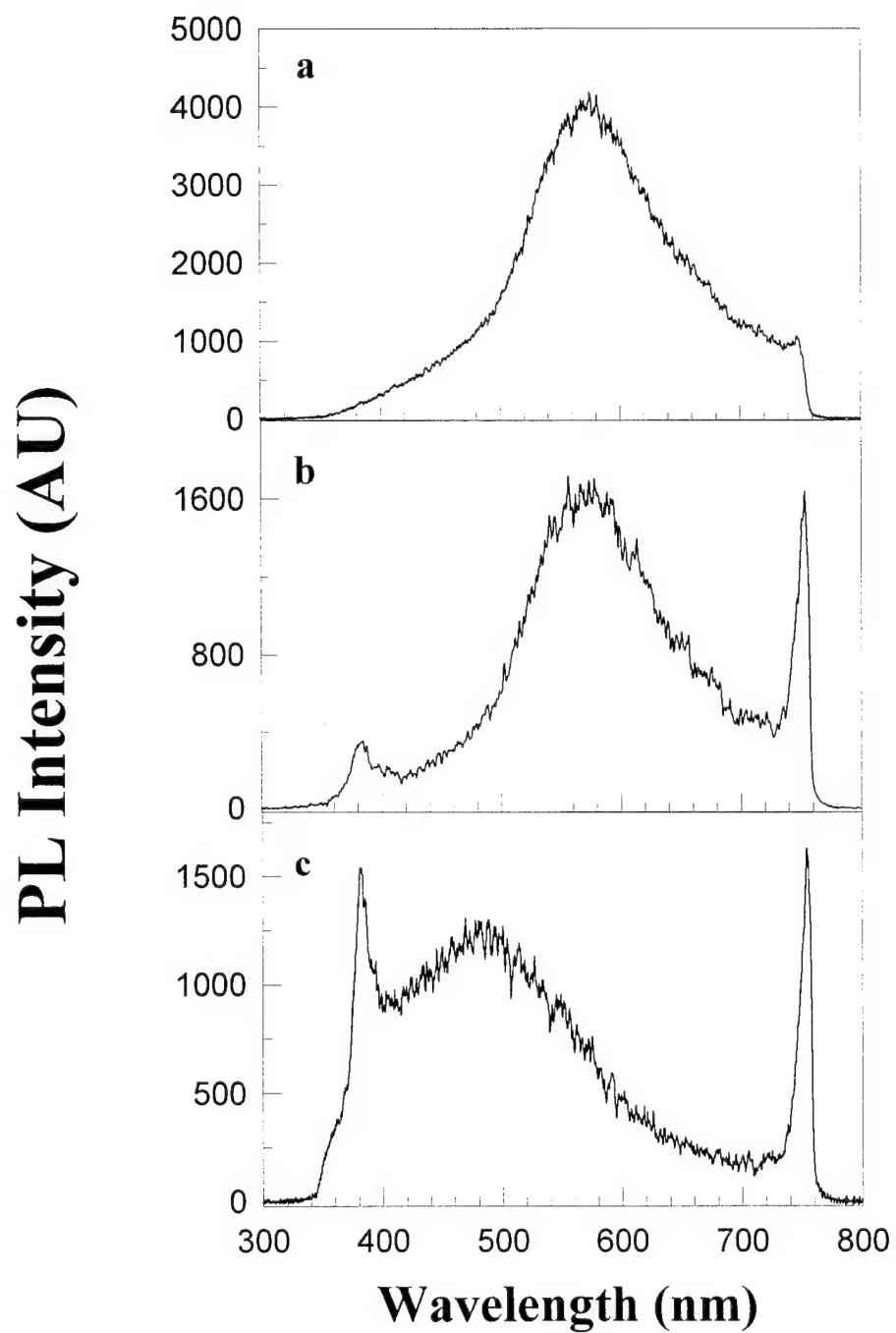
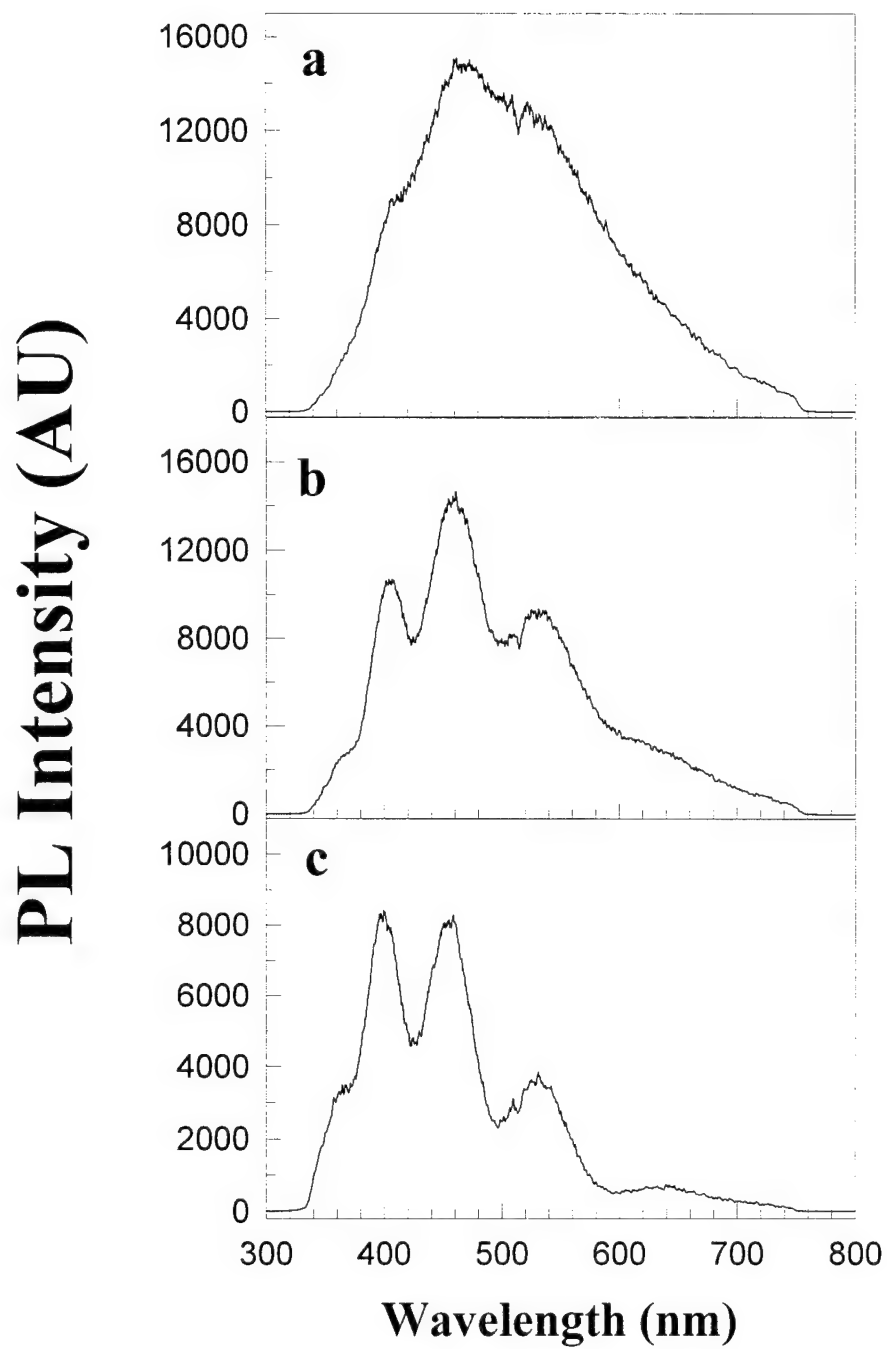Fig. 16 PL measurements from KOH-etched wires at CW 257-nm excitation

Fig. 17 PL measurements from KOH-etched wires at CW 257-nm excitation showing multiple peaks.
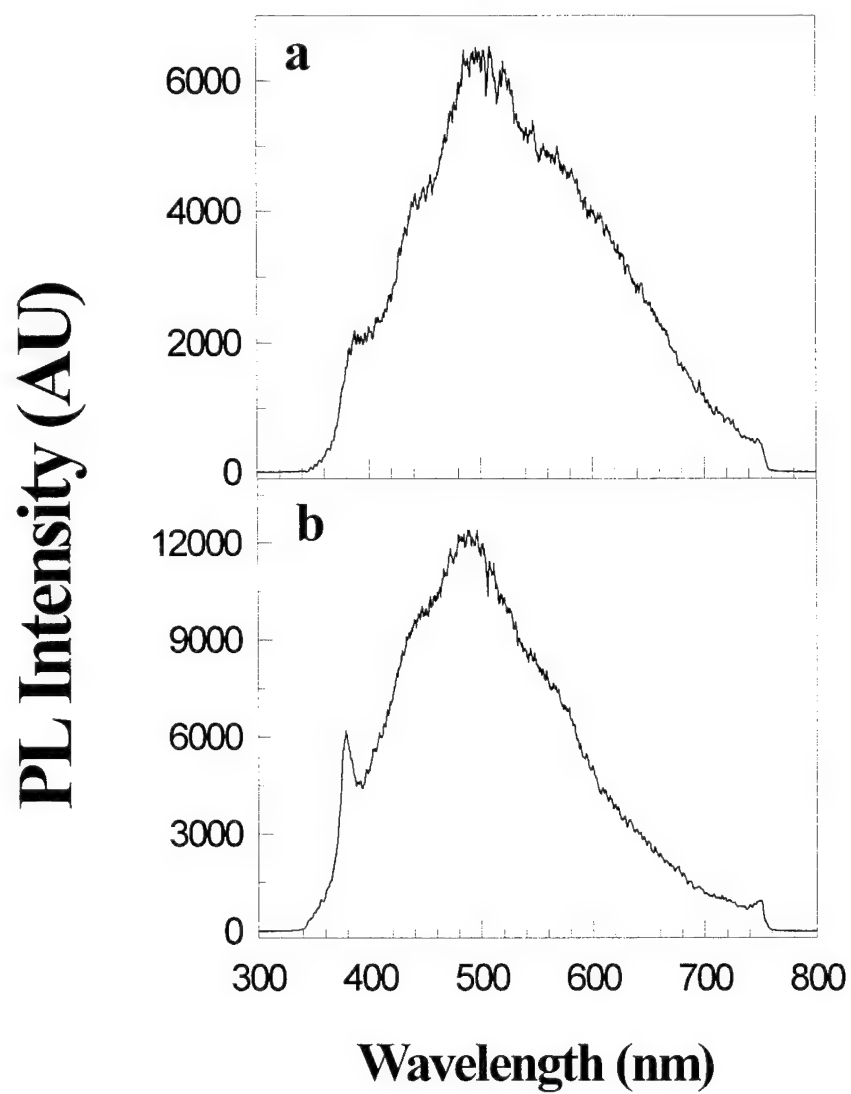
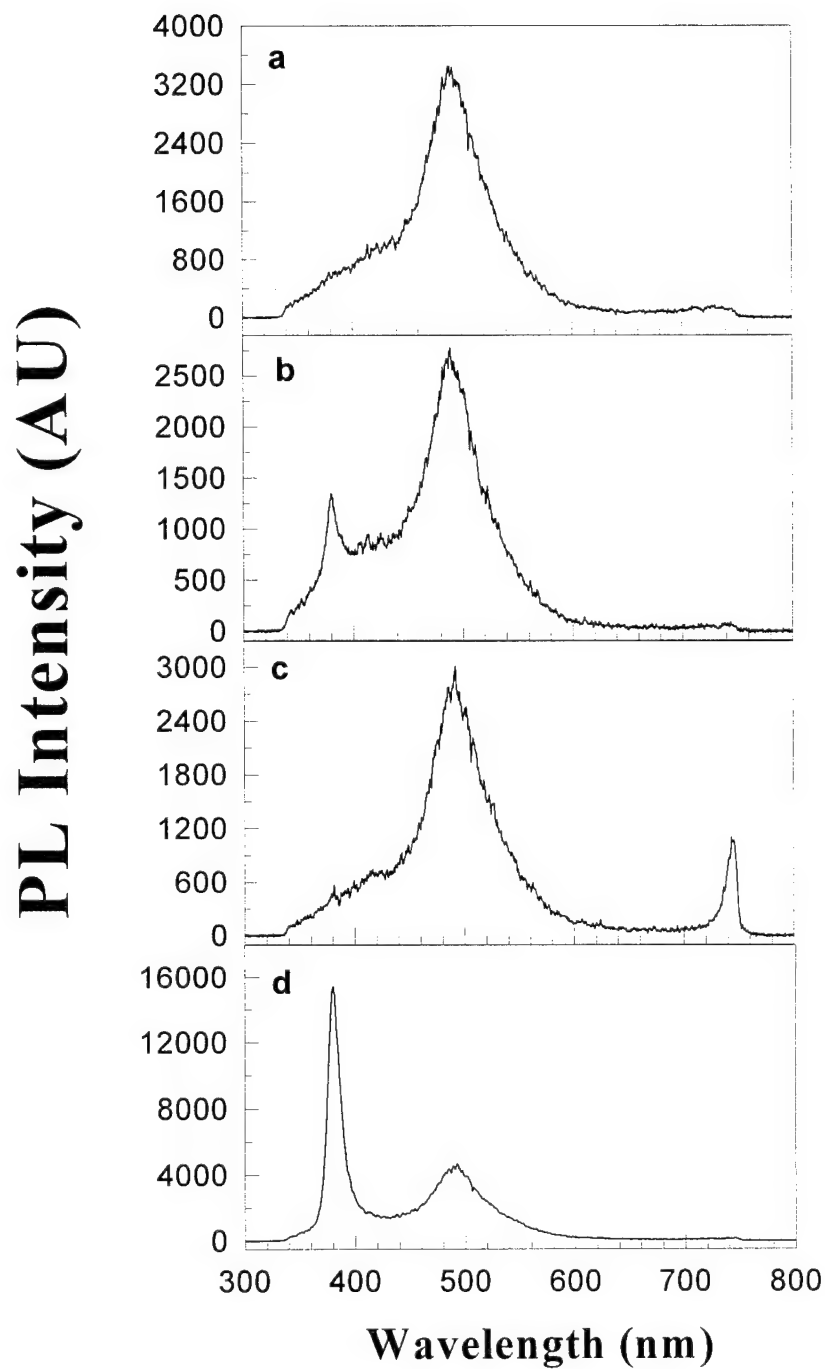Fig. 18 PL measurements from RIE wires at CW 257-nm excitation.

Fig. 19 PL measurements from RIE wires at CW 257-nm excitation.

Spectral features shown in Figs. 16-19 represent the PL characteristic of these wires, same PL lineshapes are observed irrespective of the wire profile, or the etching method. For some wires, we also observed PL peaks in 650-700 nm range. Figs. 20 & 21 show two examples of such lineshapes. Fig. 20 shows a single strong peak at ~ 680 nm with a FWHM ~ 100 nm. Fig. 21 shows both the red ~ 680 nm, and blue peaks ~ 420 nm. The blue peak is similar to the spectral features seen earlier in Figs. 17 b&c. We have also done some measurements in near IR range. At these wavelengths, the detector responsivity is much weaker in comparison with the visible range. Fig. 22 shows two examples of relatively broad PL with peaks varying from 820-880 nm. Fig. 23 shows similar PL from a different sample with a weak PL peak at ~ 860 nm, the strong line at 760 nm represents the second order of the 380-nm line observed earlier in Figs. 16-19.

These PL measurements are in good agreement with the PL measured by us from ~ 5-10 nm grating structures fabricated in (110) and (100) Si [37-38], and by 2-D Si pillars by Nassiopolous et al. [39]. The sharp line at ~ 380 nm has also been observed in the grating structures. The spectral lineshape of the 380-nm line is similar to the 340-nm σ-σ* excitonic emission from linear Si polymer chains [40]. Before, we go into the details of the PL results, it is instructive to briefly review some relevant features of the PL from π-Si and spherical Si particles. Tischler et al. [41] showed that simultaneous exposure to O_2 and laser illumination quenched red emission from π-Si. Also, Robinson et al. [4] showed that thermal annealing of π-Si in ultra-high vacuum resulted in quenching of the red emission. Yamada and Kondo [42] investigated the effects of vacuum annealing and dry oxidation on PL variation of π-Si. They showed that PL efficiency was reduced between 400-800° C, and completely quenched at ~ 1000° C processes. Petrova-Koch et al. [9] reported similar results with rapid thermal oxidation. In a model developed by Petrova-Koch et al. [9] and Qin et al. [43], the quantum size is believed to be responsible for the absorption with the surface states implicated in the emission process. Thus, the temperature-related quenching is due to rearrangement of surface states that were originally responsible for the PL. Hartstein et al. [44] showed that species such as SiOH, H_2O, and SiH_x complexes are desorbed from the surface at temperatures ~ 1000° C. Therefore, in π-Si, it is likely that $Si:H_x$ surface states in combination with nanoscale crystalline structures are responsible for the red emission. This PL model is also supported by the visible, wideband (up to 520 nm) optical emission reported by Furukawa et al. [45] from 2-5 nm diameter crystalline Si particles surrounded by $=SiH_2$ groups. Dinh et al. [46] have also reported 500-600 nm emission from 3-5 nm Si particles exposed to ambient air for extended periods; as-grown cluster samples, formed in UHV by laser ablation of a Si target, did not show any luminescence.

For the wire PL, $Si:H_x$ complexes are absent from freshly oxidized wires, also the nanoscale-linewidth Si crystalline structures are passivated by the thermally grown oxide. The broad PL in 400-570 nm range is similar to the blue emission reported from oxidized π-Si. Following extended air exposure, the $Si:H_x$ complexes are formed that should give red emission. This happens for the wire structures leading to peaks varying from ~ 680-860 nm as shown in Figs. 20-23. The 380-nm line also evolves following air exposure.
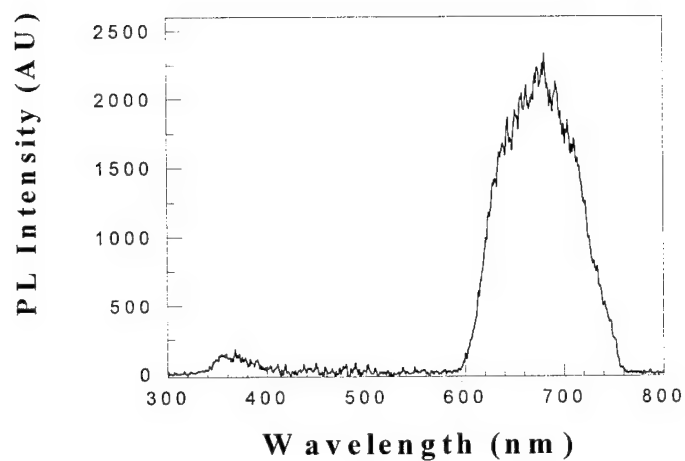
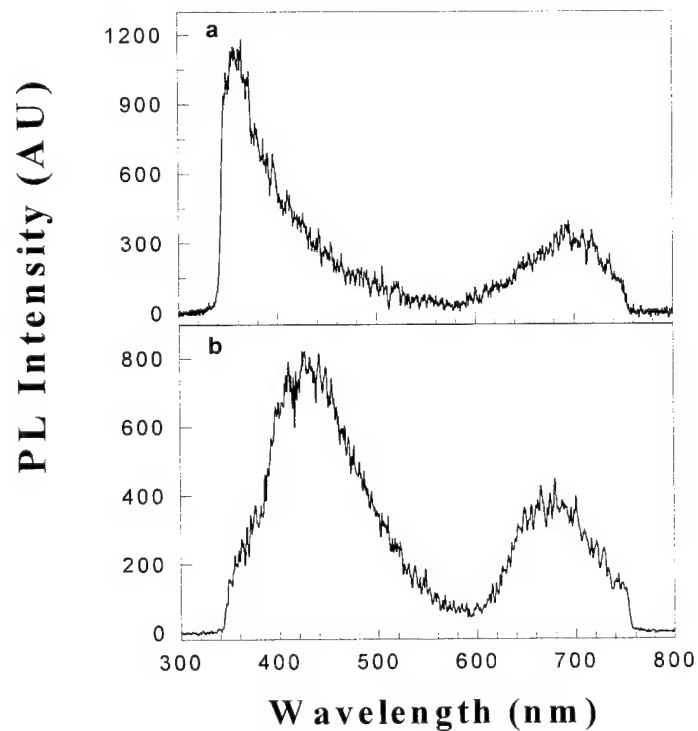Fig. 20 PL measurement from KOH-etched wires showing a peak ~ 680 nm.

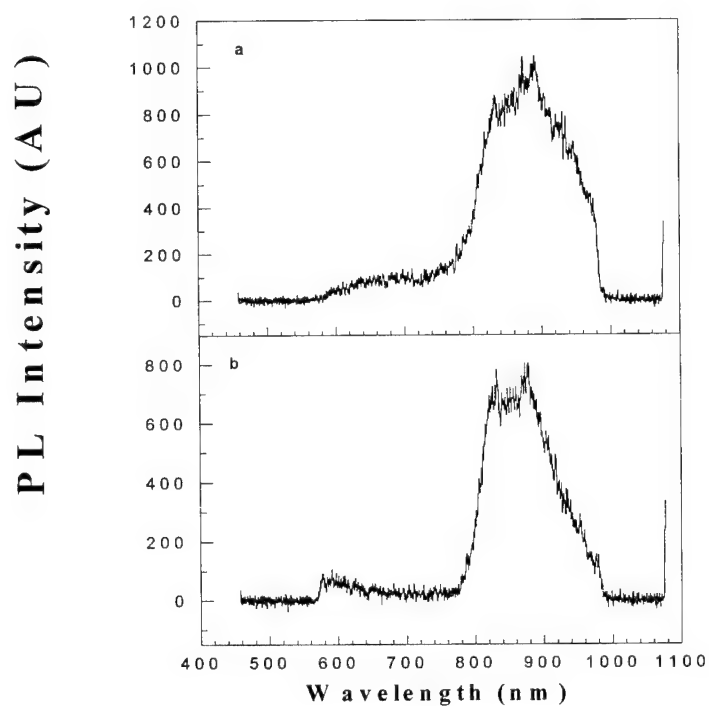Fig. 21 PL measurements from RIE wires (a) and KOH wires (b) showing peaks varying from 700-420 nm.

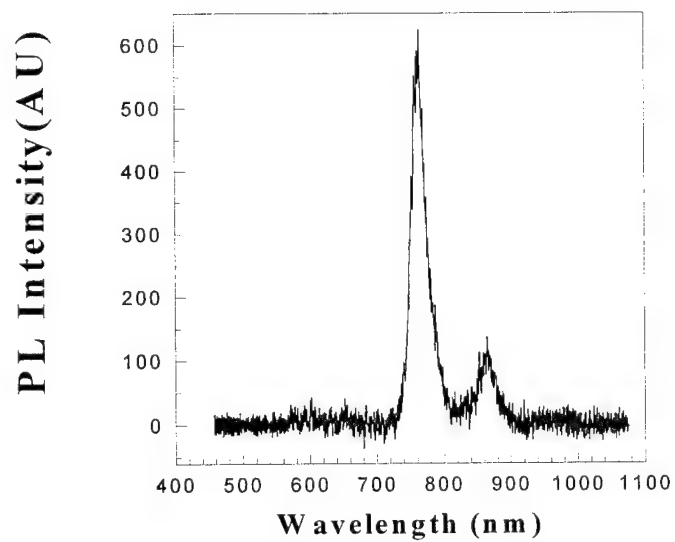Fig. 22 PL measurements from KOH-etched wires showing peaks ~ 860-880 nm.

Fig. 23 PL measurement from RIE wires showing 860-nm peak, the strong peak is the second order of the 380-nm line.

Therefore, annealing in N_2 atmosphere at ~ 1000 ° C should result in quenching of all these lines. This quenching has been observed by us for both the grating and wire structures. The broad PL at ~ 500 nm, however, is not quenched by annealing. Fig. 24 shows an example of the PL variation from RIE wires subjected to 1000° C N_2 annealing for ~ 1/2 hour. The measurements shown were taken before and after annealing. The comparison shows that the PL peak is up-shifted by about 40 nm, also the PL intensity at ~ 400 nm before annealing is significantly reduced. We have also investigated PL from as-grown oxide films [37], the PL from oxide films subjected to extended air exposure show PL peaks at ~ 490 nm, with FWHM ~ 60 nm, the as-grown films show no PL, and 1000 ° C N_2 annealing completely quenches PL.

In summary, these measurements show that PL from the crystalline Si wires originates from a combination of 5-10 nm crystal sizes and surface Si atoms passivated either by Oxygen, or $Si:H_x$ complexes giving rise to blue-green and red emission lines respectively. A more detailed understanding of the physical mechanisms will emerge by a continuation of this work by PL lifetime measurements at different emission wavelengths to determine carrier recombination mechanisms.
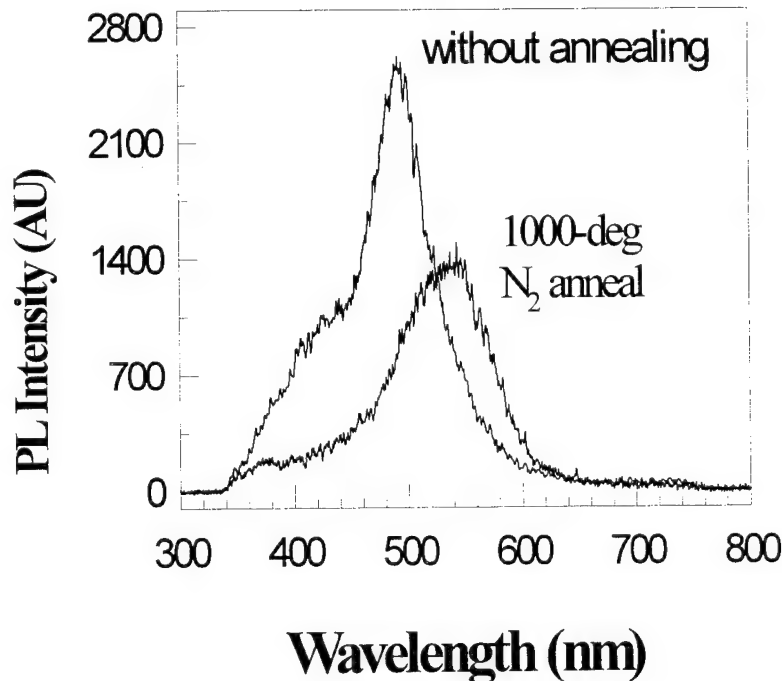

Fig. 24 Variation of PL with 1000° C N_2 annealing.

5. Electrical Characterization

The room temperature PL measurements from Si wires demonstrated their potential for optoelectronics device applications. In our phase I proposal, we had proposed to test crystalline Si wires in MSM configuration. However, from a technological point of view, it was important to determine whether the PL from the wires can be electrically excited. We, therefore, focused on incorporating pn-junctions in our nanoscale wire devices. The drawing below shows the design of the device structure. We formed crystalline Si wires in p-type regions. Both the contact regions were diffused n-type. Al films were deposited on n-type contact regions and annealed at ~ 400 ° C in

| n-type contact | p-type Si wires embedded in oxide | n-type contact |
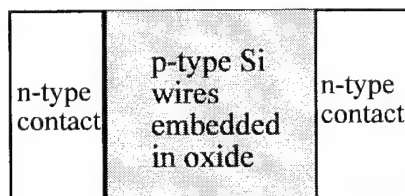
ambient N_2 atmosphere to form Ohmic contacts. Si wires in the p-type region were embedded in thermally grown oxide films to reduce their diameters to ~ 20-30 nm before visible electroluminescence (EL) was observed from these structures. Electrical characterization of this type of simple device structure in SOI configuration is straightforward, since the electrical isolation from the Si substrate underneath is provided by the thick SiO_2 film. Fig. 25a shows the visible EL from the intersection between the contact pad and wires at the right contact area. Fig. 25b shows the EL from the left contact area following reversal of polarity. Fig. 25c shows the result of image subtraction of Figs. 25 a & b showing simultaneous emission from the respective contact areas. The light emission was visible to naked eyes, and was yellow in color. The pictures shown in Fig. 25 were taken by a CCD camera in black & white, and were converted to color format using a simple grey scale to color conversion algorithm (the optical spectra was also recorded, and will be discussed later). The EL from these devices was stable under continuous current flow for as long as 90 minutes without any degradation. A large number of devices with active wire areas varying from 10 to 80 μm^2 and periods from 0.75 to 2.0 μm were fabricated and characterized. In all cases similar EL was measured, although a large variation in currents and voltages at EL was observed.

IV measurements were carried out using a Tektronix 370 curve tracer that was interfaced to a computer. Fig. 26 shows IV measurements for the EL device structure shown in pictures of Fig. 25. Fig. 26a shows AC measurements that depict a slightly asymmetric behavior. For an ideal back-to-back pn junction diode structures, IV characteristic should have been identical in both polarities. Fig. 26b shows IV measurement at EL in +DC polarity, the onset of EL is the curvature of the IV plot identified by an arrow. Fig. 26c shows IV measurements at EL in -DC polarity. In both cases, the EL is observed for the junction under forward bias, i.e., the contact at which light is observed (left, or right) is biased negative, while the other contact is biased

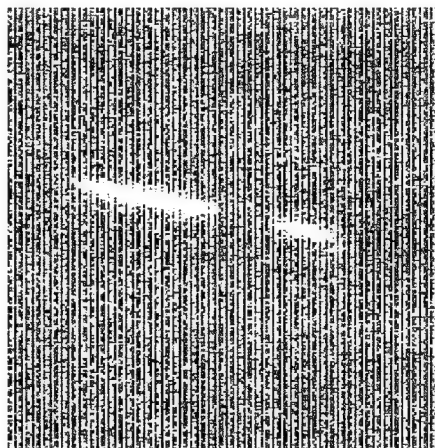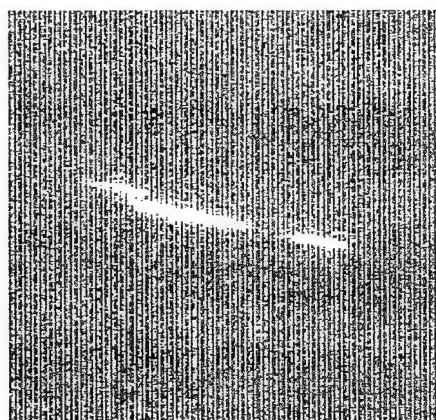Fig. 25a CCD picture of a luminescent Si device, emission is from right contact area.

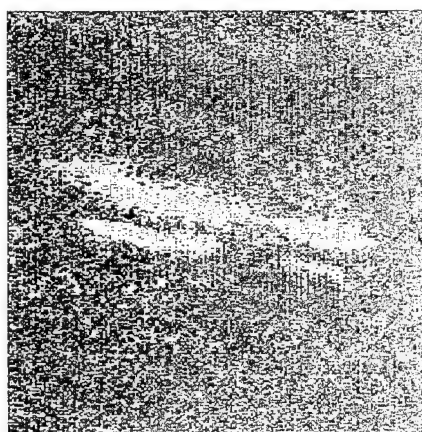Fig. 25b CCD picture of a luminescent Si device, emission is from left contact area.

Fig. 25c Image subtraction of CCD pictures shown in Figs. 25 a & b showing light emission from the two respective pn-junction contact areas.
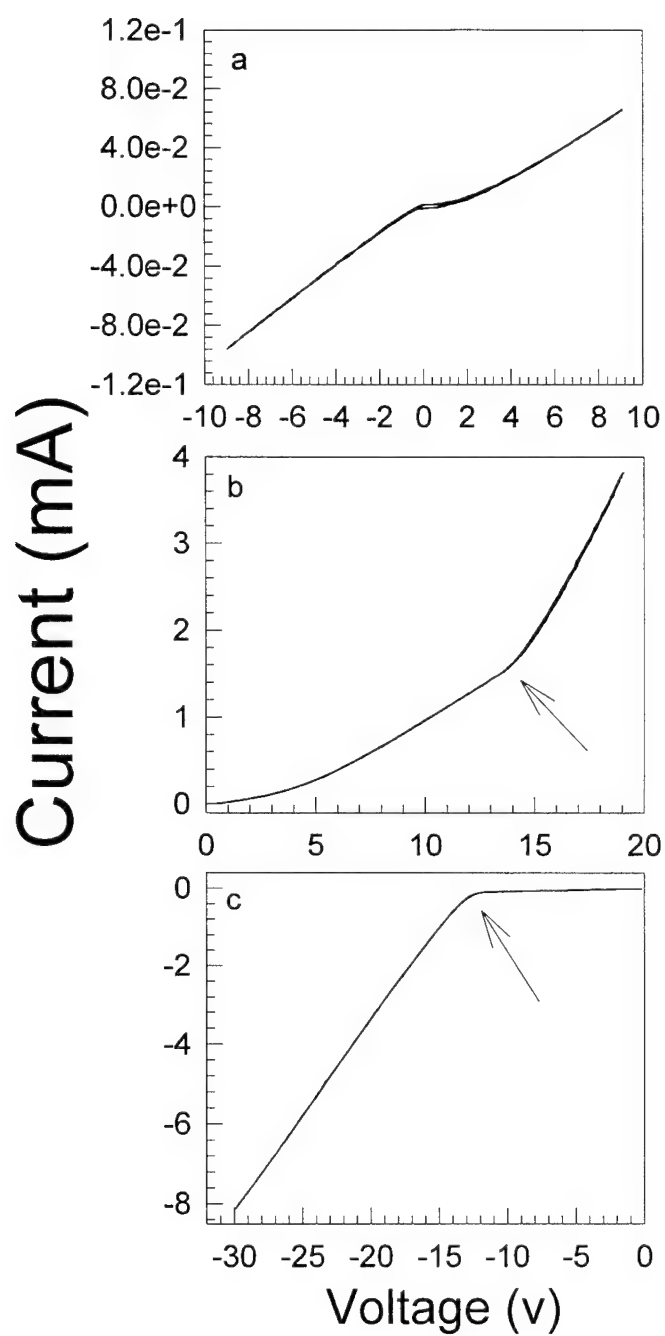
Fig. 26 IV measurements from luminescent devices, a) AC mode, b) + DC, and c) -DC mode.

positively, i.e., the contact without any EL. We observed very little EL under reverse-bias conditions. The EL spectra was measured by coupling device light into a fiber that was connected to a monochromator. Fig. 27 shows a typical EL measurement exhibiting a strong peak at ~ 650 nm, with shoulders at ~ 520 and 720 nm. The transmission through the fiber was calibrated using a He-Ne laser line and also by measuring spectra from a wide-band light source. However, the transmission at shorter wavelengths was not calibrated. Thus, it is possible that short-wavelength of the EL spectra may be absorbed in the fiber. More experiments are in progress to directly introduce light from the device to the monochromator.
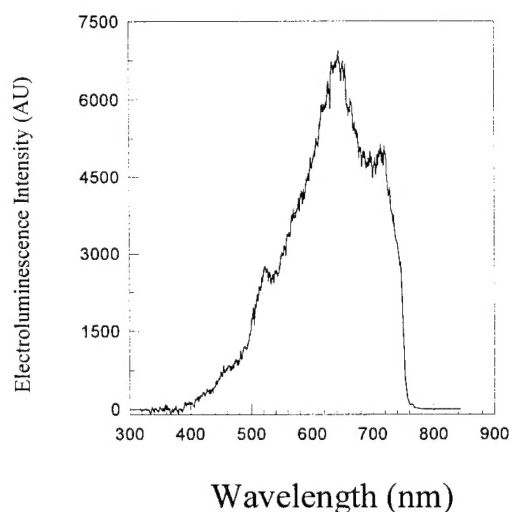

Fig. 27 EL measurement under forward bias for the device shown in Fig. 25.

Light emission from crystalline Si under reverse bias conditions has been previously reported [47]. This light emission was attributed to radiative relaxation mechanisms involving high energy carriers in the avalanche breakdown. In crystalline Si, light emission under forward bias conditions has not been observed. Many reports of EL from porous Si under forward bias conditions have been reported. Richter et al. [48] reported EL from π-Si at high voltages (~ 200 V) under both forward and reverse bias conditions. The measured EL spectrum showed a peak at ~ 650 nm. Koshida et al. [49] showed that significant EL from π-Si was measured only under forward bias conditions, their EL showed a peak at ~ 700 nm, and their IV characteristics were similar to our measurements. Kesan et al. [50] also showed that EL from π-Si was measured only under forward bias conditions, their EL spectral shape was broad with shoulders at ~ 650 and 780 nm. Their turn-on voltages were very small (0.7-1 v), at least an order of magnitude smaller than our results, the characteristic IV lineshape, however, was the same.

A comparison of π-Si and wire EL shows that the emission spectra and IV characteristics are similar. In contrast with π-Si, wire structures are a lot more uniform,

possesscrystalline structure, and are passivated by thermally grown oxide. We believe that these are the first reported EL measurements from non-porous crystalline Si structures under forward bias conditions. A number of issues need to be investigated before the exact origin of this EL can be established. Phase II effort will focus on such pertinent issues as exact wire diameters at the onset of EL, passivation by hydrides, and optimum junction configuration.

6. Discussion

The primary objective of phase I SBIR project was to try and understand the physical mechanisms responsible for room temperature PL in π-Si. The strategy was that by using a more uniform and controlled lithographic fabrication approach, Si crystalline wires can be fabricated and systematically reduced to quantum sizes ($\sim$ 5-10 nm) by using controlled oxidation processes. Si wires in SOI configuration offered a unique material system for both optical and electrical characterization. During the course of the phase I research, we developed nanofabrication techniques that were applicable not only to SOI but also to the conventional Si wafers. Raman scattering and SEM measurements were extensively used to characterize both the wires and grating structures as the crystalline dimensions were reduced to $\sim$ 10 nm. RS results for wires were in good agreement with our grating results and the data reported in literature. One major exception, however, was the un-explained high-frequency shift of the bulk Raman mode. This shift appears related to compressive stress, and needs to be investigated in more detail. For wire diameters < 20 nm, RS and SEM measurements are not inappropriate. In SEM measurements, the focused electron beam tends to oxidizes rest of the Si before a picture can be acquired. This is also caused by the lack of efficient heat conduction of the wires embedded in oxide films. Raman scattering measurements are inapplicable because of the long time of scan ($\sim$ 10 minutes) in which a focused laser beam stays on the wires and causes Si oxidation. This issue, however, can be resolved by employing real-time Raman scattering systems that have the requisite resolution.

The room temperature PL measurements showed two bands : red and blue-green emission, which have been observed from the as-prepared and oxidized porous Si respectively. Our work showed that nanoscale structures are required for the visible PL. The red emission is due to surface states associated with Si-Hydrogen complexes. Blue-green emission is not from oxide films as has been suggested by some researchers. We have always observed this emission either from as-prepared samples, or from thermally annealed samples which quenches the red emission. A very promising feature of our PL measurements was the emergence of a sharp line at $\sim$ 380-nm that is also associated with Si-Hydrogen complexes. The first-principles calculations predict crystal sizes $\sim$2-3 nm for blue-green emission. Our results show crystal sizes to be $\sim$ 10 nm at the onset of PL. This discrepancy may be attributed to the presence of steps on sidewalls (see Figs. 2 & 3) that are characteristic of the etching process. For wire linewidths of $\sim$ 10-20 nm, these steps introduce size variations of $\sim$ 2-3 nm, and may be responsible for the PL. A better clarification of this issue requires extensive transmission electron microscope studies.

The existence of stable EL from these wires is a strong manifestation of the changed physical properties of Si at crystalline dimensions < 20 nm. According to the SEM measurements of the EL devices, the wire diameters were ~ 20-30 nm, which is too large for PL effects. Again, it is likely that the sidewall steps are playing a role in the EL.

In summary, phase I results have demonstrated a number of interesting physical properties in crystalline Si material as the crystal sizes are reduced to ~ 10 nm. The device potential of Si nanostructures is established by stable EL measurements under forward-bias conditions. More rigorous experimental and theoretical efforts are required before these extraordinary changes in Si physical properties can be understood and their considerable commercial potential realized.

7. References

1. L. T. Canham, Appl. Phys. Lett. **57**, 1046 (1990).
2. C. Pickering, M. I. J. Beale, D. J. Robbins, P. J. Pearson, and R. Greef, Thin Solid Films **125**, 157 (1985).
3. V. Lehman and U. Gosele, Appl Phys. Lett. **58**, 856 (1991).
4. M. B. Robinson, A. C. Dillon, D. R. Haynes, and S. M. George, Appl. Phys. Lett. **61**, 1414 (1992).
5. V. Petrova-Koch, T. Muschik, A. Kux, B. K. Meyer, F. Koch, and V. Lehman, Appl. Phys. Lett. **61**, 943 (1992).
6. Y. Kanemitsu, T. Ogawa, K. Shiraishi, and K. Takeda, Phys. Rev. **B 48**, 4883 (1993).
7. M. S. Brandt, H. D. Fuchs, M. Stutzman, J. Weber, and M. Cardona, Solid State Commun. **81**, 307 (1992).
8. A. Roy, A. Chaimani, D. D. Sarma, and A. K. Sood, Appl. Phys. Lett. **61**, 1655 (1992).
9. F. Koch, V. Petrova-Koch, and T. Muschik, Jour. of Lumin. 57, 271 (1993).
10. D. I. Kovalev, I. D. Yaroshetzki, T. Muschik, V. Petrova-Koch, and F. Koch, Appl. Phys. Lett. **64**, 214 (1994).
11. S. M. Prokes, Appl. Phys. Lett. **62**, 3244 (1994).
12. D. J. Lockwood, Solid State Commun. **92**, 101 (1994).
13. H. Liu, D. K. Biegelsen, N. M. Johnson, F. A. Ponce, and R. F. W. Pease, Jour. Vac. Sci. Technol. **B 11**, 2352 (1993).
14. P. B. Fischer, K. Dai, E. Chen, and S. Y. Chou, Jour. Vac. Sci. Technol. **B 11**, 2524 (1993).
15. Saleem H. Zaidi and S. R. J. Brueck, Appl. Opt. **27**, 2999 (1988).
16. Saleem H. Zaidi and S. R. J. Brueck, Jour. Vac. Sci. Technol. **B 11**, 658 (1993).
17. E. Bassous, IEEE Trans. Elec. Dev., **ED-25**, 1178 (1978).
18. K. E. Bean, IEEE Trans. Elec. Dev., **ED-25**,1185 (1978).
19. A. Malag, Opt. Commun. **32**, 54 (1980).
20. D. L. Kendall, Jour. Vac. Sci. Technol. **A 8**, 3598 (1990).
21. An-Shyang Chu, Saleem H. Zaidi, and S. R. J. Brueck, Appl. Phys. Lett. **63**, 905 (1993).
22. D-B Kao, J. P. McVittie, W. P. Nix, and K. C. Saraswat, IEEE Trans. Elect. Dev., **ED-34**, 1008 (1987).

23. A. Potts, D. G. Hasko, J. R. A. Cleaver, and H. Ahmed, Appl. Phys. Lett. **52**, 834 (1988).

24. A. Potts, D. A. Williams, R. J. Young, R. J. Blaikie, R. A. McMahon, D. G. Hasko, J. R. A. Cleaver, and H. Ahmed, Jpn. Jour. Appl. Phys. **29**, 2675 (1990).

25. K. Itoh, K. Iwameji, and Y. Sasaki, Jpn. Jour. Appl. Phys. **30**, L 1605 (1991).

26. R. Tsu, H. Shen, and M. Dutta, Appl. Phys. Lett. **60**, 112 (1992).

27. S. R. Goodes, T. E. Jenkins, M. I. J. Beale, J. D. Benjamin, and R. C. Pickering, Semicond. Sci. Technol. **3**, 483 (1987).

28. T. Kanata, H. Murai, and K. K. Kubota, Jour. Appl. Phys. **61**, 969 (1987).

29. N. Ohtani and K. Kanamura, Solid State Commun. **75**, 711 (1990).

30. Z. Iqbal and S. Veprel, J. Phys. **C:15**, 377 (1982).

31. M. Chandrasekhar, H. R. Chandrasekhar, M. Grimsditch, and M. Cardona, Phys. Rev. **B 22**, 4825 (1980).

32. F. Cerdeira, T.A. Fjeldy, and M. Cardona, Phys. Rev. **B 10**, 4344 (1974).

33. F. Moser and R. Beserman, Jour. Appl. Phys. **54**, 1033 (1983).

34. M. Kanamura, Y. Kobayashi, and K. Usani, Jpn. Jour. Appl. Phys. **23**, 687 (1984).

35. J. F. Morhange, G. Kanellis, and M. Balkanski, Solid State Commun. **31**, 805 (1979).

36. G. Kanellis, J. F. Morhange, and M. Balkanski, Phys. Rev. **B 21**, 1543 (1980).

37. Saleem H. Zaidi, An-Shyang Chu, and S. R. J. Brueck, Optical Properties of Nanoscale, One-dimensional Silicon Grating Structures, submitted for publication to Phys. Rev. B (Nov., 1995).

38. Saleem H. Zaidi and S. R. J. Brueck, Photoluminescence of Manufactured 1-D Crystalline Si Gratings, submitted to Phys. Rev. Lett. (Jan., 1996).

39. A. G. Nassiopoulos, S. Grigoropoulos, and D. Papadimitriou, Light emitting properties of Si Nanopillars produced by lithography and etching, Proc. Elect. Chem. Soc. Meet., Oct. 1995.

40. W. L. Wilson and T. W. Weidman, J. Phys. Chem. **95**, 4568 (1991).

41. M. A. Tischler, R. T. Collins, J. H. Stathis, and J. C. Tsang, Appl. Phys. Lett. **60**, 639 (1992).

42. M. Yamada and K. Kondo, Jpn. J. Appl. Phys. **31**, L993 (1992).

43. G. G. Qin and Y. Q. Jia, Solid State Commun. **86**, 559 (1993).

44. A. Hartstein, D. J. DiMaria, D. W. Dong, and J. A. Kucza, J. Appl. Phys. **51**, 3860 (1980).

45. S. Furukawa and T. Miyasato, Jpn. J. App. Phys. **27**, L2207 (1988).

46. L. N. Dinh, L. L. Chase, M. Balooch, L. T. Terminello, and F. wooten, Appl. Phys. Lett. **65**, 3111 (1994).

47. R. Newman, Phys. Rev. **100**, 700 (1953).

48. A. Richter, P. Steiner, F. Kozlowski, and W. lang, IEEE Trans. Elec. Dev. Lett. **12**, 691 (1991).

49. N. Koshida and H. Koyama, Appl. Phys. Lett. **60**, 347 (1992).

50. V. P. Kesan, E. Bassous, P. Munguia, S. F. Pesarcik, M. Freeman, S. S. Iyer, and J. M. Halbout, J. Vac. Sci. Technol. **A 11**, 1736 (1993).